communications physics

ARTICLE

https://doi.org/10.1038/s42005-022-00812-7 OPEN

Protocol designs for NOON states

Daniel S. Grün[1], Karin Wittmann W.[1], Leandro H. Ymai[2], Jon Links[3✉] & Angela Foerster[1]

The ability to reliably prepare non-classical states will play a major role in the realization of quantum technology. NOON states, belonging to the class of Schrödinger cat states, have emerged as a leading candidate for several applications. Here we show how to generate NOON states in a model of dipolar bosons confined to a closed circuit of four sites. This is achieved by designing protocols to transform initial Fock states to NOON states through use of time evolution, application of an external field, and local projective measurements. The evolution time is independent of total particle number, offering an encouraging prospect for scalability. By variation of the external field strength, we demonstrate how the system can be controlled to encode a phase into a NOON state. We also discuss the physical feasibility, via ultracold dipolar atoms in an optical superlattice setup. Our proposal showcases the benefits of quantum integrable systems in the design of protocols.

[1] Instituto de Física da UFRGS, Av. Bento Gonçalves 9500, Agronomia, Porto Alegre, RS 91501-970, Brazil. [2] Universidade Federal do Pampa, Av. Maria Anunciação Gomes de Godoy 1650, Malafaia, Bagé, RS 96413-170, Brazil. [3] School of Mathematics and Physics, The University of Queensland, Brisbane, QLD 4072, Australia. ✉email: jrl@maths.uq.edu.au

Quantum systems are widely considered to be the most promising foundation for the next generation of platforms in computing, communication, measurement, and simulation. This is primarily due to the properties of state superposition and entanglement. To realize the potential for progress, it is necessary to establish protocols that are capable of generating important quantum states.

The NOON state is a fundamental example. It is an "all and nothing" superposition of two different modes[1,2]. For N particles, it has the form

$$|\mathrm{NOON}\rangle = \tfrac{1}{\sqrt{2}}\left(|N,0\rangle + e^{i\varphi}|0,N\rangle\right) \tag{1}$$

where the phase φ typically records information in applications. These include: in the fields of quantum metrology and sensing, performing precision phase-interferometry at the Heisenberg limit[3] and overcoming diffraction limits in quantum lithography[4]; in tests of fundamental physics, NOON states are used to study Bell-type inequalities violation[5]; they offer promising applications in Quantum Communication and Quantum Computing[6], and their utilization is expected to extend to areas such as chemistry and biology[7]. After early success, using photon pairs and Hong-Ou-Mandel (HOM) interferometry[8], several schemes have followed for the production and detection of photonic NOON states[2,9–12]. There are also proposals using other architectures, such as circuit QED[13], trapped ions[14], and Bose-Einstein condenstates[15].

The creation of Bose-atom NOON states would enable new tests, using massive states, of the foundations for quantum mechanics. A step in this direction was taken with the demonstration of the matter-wave equivalent of the HOM effect[16,17]. Prospects for creating Bose-atom NOON states using a double-well potential were first floated some time ago[18]. This early work considered an attractive system, which is prone to instability. In principle, a more robust repulsive system can be prepared to evolve to a high-fidelity approximation of a NOON state. However, the drawback here is that the process is associated with an extremely large time scale. Recently, new studies of the double-well system have been undertaken to reduce the time scale. One example proposes to adiabatically vary the system parameters through an excited-state phase transition during the process[19]. Another study employs periodic driving to lower the NOON-state evolution time[20]. Nonetheless, the time to generate a NOON state in these examples still, increasingly, scales with the total number of particles.

Here we present an alternative to circumvent these issues. Our approach adopts a closed-circuit of four sites, with a Fock-state input of M particles in site 1, P particles in site 2, and no particles in sites 3 and 4, denoted as $|\Psi_0\rangle = |M,P,0,0\rangle$. The initial step is to create an uber-NOON state, with the general form

$$|\,\text{u-NOON}\,\rangle = \frac{1}{2}\left(|M,P,0,0\rangle + e^{i\varphi_1}|M,0,0,P\rangle + e^{i\varphi_2}|0,P,M,0\rangle + e^{i\varphi_3}|0,0,M,P\rangle\right)$$

for a set of phases $\{\varphi_1, \varphi_2, \varphi_3\}$. This state may be viewed as an embedding of NOON states (1) within two-site subsystems. We then describe two protocols to extract a NOON state from an uber-NOON state, one through dynamical evolution followed by local projective measurement and post-selection, the other from dynamical evolution alone. The protocols are schematically presented in Fig. 1.

The approach taken has the following properties: (i) The system has long-ranged interactions, described by the Extended Bose-Hubbard Model (EBHM)[21]. There exists a choice of the coupling parameters for which this model is integrable[22]. As in other physically realized integrable systems[23–30], this property facilitates several analytic calculations for physical quantities. Here, integrability exposes the protocols available for NOON state generation. The execution time is found to be dependent on the difference between the two initially populated sites within the four-site system. It is independent of total particle number, opening a means for scalability.

(ii) The system can be controlled by breaking the integrability over small time scales. Encoding of the phase into a NOON state only requires breaking of integrability over an interval that is several orders of magnitude smaller than the entire execution time. This causes minimal loss in fidelity. (iii) With currently available technology, the system may be realized and controlled using dipolar atoms (e.g., dysprosium or erbium) with repulsive interactions, trapped in optical lattices[31,32]. In this setup, the evolution times that we compute for NOON-state generation are of the order of seconds.

For the four-site configuration, the EBHM Hamiltonian is

$$H = \frac{U_0}{2}\sum_{i=1}^{4} N_i(N_i-1) + \sum_{i=1}^{4}\sum_{j=1,j\neq i}^{4}\frac{U_{ij}}{2}N_iN_j - \frac{J}{2}\left[(a_1^\dagger + a_3^\dagger)(a_2 + a_4) + (a_1 + a_3)(a_2^\dagger + a_4^\dagger)\right], \tag{2}$$

where $a_j^\dagger$, a_j are the creation and annihilation operators for site j, and $N_j = a_j^\dagger a_j$ are the number operators. The total number operator $N = N_1 + N_2 + N_3 + N_4$ is conserved. Above, U_0 characterizes the interaction between bosons at the same site, $U_{ij} = U_{ji}$ is related to the long-range (e.g., dipole-dipole) interaction between bosons at sites i and j, and J accounts for the tunneling strength between different sites.

Below, we describe two protocols that enable the generation of NOON states, with fidelities greater than 0.9. A physical setup to implement them is also discussed.

Results

Insights into the physical behavior of Eq. (2) become accessible at the integrable coupling. Setting $U_{13} = U_{24} = U_0$ and $U_{12} = U_{23} = U_{34} = U_{14}$, the system acquires two additional conserved quantities, Q_1 and Q_2, such that $2Q_1 = N_1 + N_3 - a_1^\dagger a_3 - a_1 a_3^\dagger$ and $2Q_2 = N_2 + N_4 - a_2^\dagger a_4 - a_2 a_4^\dagger$. Together with the total number of particles N and the Hamiltonian H, the system possesses four independent, conserved quantities. This is equal to the number of degrees of freedom, satisfying the criterion for integrability. Suppose that, initially, there are M atoms in site 1 and P atoms in site 2. We identify the resonant tunneling regime as being achieved when $U|M-P| \gg J$ (see Methods for details), where $U = (U_{12} - U_0)/4$. This regime is characterized by sets of bands in the energy spectrum (see Supplementary Note 1). In this region, an effective Hamiltonian H_{eff} (see Methods, Eq. (3)) enables the derivation of analytic expressions for several physical quantities.

In the settings discussed above, the system described by Eq. (2) provides the framework to generate uber-NOON states when $N = M + P$ is odd[33]. To encode phases, however, it is necessary to break the integrability in a controllable fashion. Here, we introduce two idealized protocols to produce NOON states with general phases by breaking the system's integrability with externally applied fields. We call the subsystem containing sites 1, 3 as A, and the one containing sites 2, 4 as B. We denote three time intervals: t_{m}, t_μ, and t_ν. The first, corresponding to integrable time evolution, is associated with evolution to a particular uber-NOON state. The others, associated with smaller-scale non-integrable evolution, produce phase encoding. Both protocols are built around a general time-evolution operator

$$\mathcal{U}(t,\mu,\nu) = \exp\left(-\frac{it}{\hbar}[H + \mu(N_2 - N_4) + \nu(N_1 - N_3)]\right),$$

where the applied field strengths μ, ν implement the breaking of

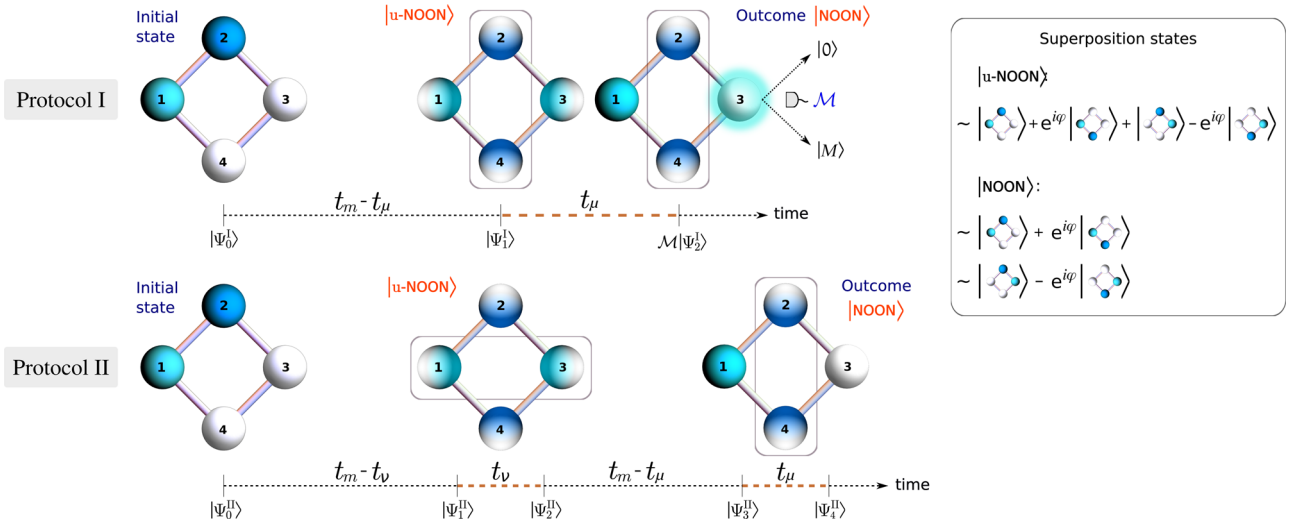

Fig. 1 NOON state generation scheme. The four spheres on the left represent the initial state, with white indicating an empty site. Cyan and blue correspond to *M* and *P* particles, respectively. In time-evolved states, gradient colors are used to indicate that the state of a site is entangled with the rest of the system - superposition states for each step are shown in the framed legend. The bars connecting the spheres denote tunneling between nearest-neighbor sites, while the rectangles represent applied external fields to sites 1-3 (ν) and 2-4 (μ). In Protocol I, the system initially evolves for time $t_m - t_\mu$, towards the u-NOON state. Then, a field is applied across sites 2-4 for time t_μ (dashed brown time line), to encode a phase. Finally, the light cyan halo portrays a projective measurement process at site 3, denoted by $\mathcal{M}$. The outcomes $|0\rangle$ and $|M\rangle$ signify which of two possible NOON states results across sites 2-4. Similarly in Protocol II, the system first evolves for time $t_m - t_\nu$, then a field is applied to sites 1-3 for time t_ν to implement the phase $\pi/2$. Next, the system evolves for time $t_m - t_\mu$, after which a field is applied to sites 2-4 to encode a phase during time t_μ. This results in a NOON state across sites 2-4, without performing a measurement procedure.

integrability. It is convenient to introduce the phase variable $\theta = 2\mu t_\mu/\hbar$, and to fix $t_\nu = \hbar\pi/(4M\nu)$, with $\hbar$ the reduced Planck constant.

Protocol I. In this protocol we employ breaking of integrability through an applied field to subsystem *B* and a measurement process. The protocol consists of three sequential steps, schematically depicted in Fig. 1:

$$\begin{aligned}&\text{(i)} \quad \left|\Psi_1^{\mathrm{I}}\right\rangle = \mathcal{U}(t_{\mathrm{m}} - t_\mu, 0, 0)\left|\Psi_0\right\rangle;\\ &\text{(ii)} \quad \left|\Psi_2^{\mathrm{I}}\right\rangle = \mathcal{U}(t_\mu, \mu, 0)\left|\Psi_1^{\mathrm{I}}\right\rangle;\\ &\text{(iii)} \quad \left|\Psi_3^{\mathrm{I}}\right\rangle = \mathcal{M}\left|\Psi_2^{\mathrm{I}}\right\rangle,\end{aligned}$$

where $t_{\mathrm{m}} = \hbar\pi/(2\Omega)$ (see Methods) and $\mathcal{M}$ represents a projective measurement of the number of bosons at site 3 (which could be implemented, in principle, through site-selective imaging[34–36] or Faraday rotation detection[37–39]). A measurement outcome of 0 or *M* heralds a high-fidelity NOON state in subsystem *B*. For other measurement outcomes, the output is discarded and the process repeated (post-selection).

Idealized limit. There is an idealized limit for which the above protocol has perfect success probability and output fidelity. Taking $t_\mu \to 0$, $\mu \to \infty$ such that θ remains finite, and using the effective Hamiltonian, provides explicit expressions for the uber-NOON states that result at steps (i) and (ii)

$$\begin{aligned}\left|\Psi_1^{\mathrm{I}}\right\rangle = \frac{1}{2}\big(&\beta|M,P,0,0\rangle + |M,0,0,P\rangle\\ &+ |0,P,M,0\rangle - \beta|0,0,M,P\rangle\big)\\ \left|\Psi_2^{\mathrm{I}}\right\rangle = \frac{1}{2}\big(&\beta|M,P,0,0\rangle + e^{iP\theta}|M,0,0,P\rangle\\ &+ |0,P,M,0\rangle - \beta e^{iP\theta}|0,0,M,P\rangle\big)\end{aligned}$$

Note that due to the conservation of $N_1 + N_3$ and $N_2 + N_4$ under the effective Hamiltonian, Fock states such as $|M,0,P,0\rangle$ and $|0,M,0,P\rangle$ do not appear in the above expression. Next, the two possible states at step (iii) depend on the measurement outcome *r* at site 3:

$$\left|\Psi_3^{\mathrm{I}}\right\rangle = \begin{cases}\frac{1}{\sqrt{2}}\big(\beta|M,P,0,0\rangle + e^{iP\theta}|M,0,0,P\rangle\big), & r = 0,\\ \frac{1}{\sqrt{2}}\big(|0,P,M,0\rangle - \beta e^{iP\theta}|0,0,M,P\rangle\big), & r = M,\end{cases}$$

with $\beta = (-1)^{(N+1)/2}$. These states are recognized as products of a NOON state for subsystem *B* with Fock basis states for subsystem *A*.

In the non-ideal case with non-zero t_μ and finite μ, there is a small probability that the measurement outcome *r* is neither 0 or *M*. Numerical benchmarks for the measurement probabilities and NOON state output fidelities are provided in a later section. Next, we describe a second protocol.

Protocol II. Now we specify an alternative protocol that does not involve measurements, so post-selection is not required. Employing the same initial state $\left|\Psi_0\right\rangle$, the following sequence of steps are implemented to arrive at a NOON state in subsystem *B* (illustrated in Fig. 1):

$$\begin{aligned}&\text{(i)} \quad \left|\Psi_1^{\mathrm{II}}\right\rangle = \mathcal{U}(t_{\mathrm{m}} - t_\nu, 0, 0)\left|\Psi_0\right\rangle;\\ &\text{(ii)} \quad \left|\Psi_2^{\mathrm{II}}\right\rangle = \mathcal{U}(t_\nu, 0, \nu)\left|\Psi_1^{\mathrm{II}}\right\rangle;\\ &\text{(iii)} \quad \left|\Psi_3^{\mathrm{II}}\right\rangle = \mathcal{U}(t_{\mathrm{m}} - t_\mu, 0, 0)\left|\Psi_2^{\mathrm{II}}\right\rangle;\\ &\text{(iv)} \quad \left|\Psi_4^{\mathrm{II}}\right\rangle = \mathcal{U}(t_\mu, \mu, 0)\left|\Psi_3^{\mathrm{II}}\right\rangle.\end{aligned}$$

Idealized limit. Similar to Protocol I, in the limit $\mu, \nu \to \infty$, $t_\mu, t_\nu \to 0$, and implementing $\mathcal{U}(t, \mu, \nu)$ with the effective

Table 1 Fidelities for Protocols I and II.

	$F_{\rm I}$		$F_{\rm II}$	$P\theta = \pi/2$		
	$r = 0$	$r = M$		t_μ	t_ν	t_m
Set 1	0.986	0.997	0.974	0.0024 s	0.0065 s	6.1639 s
Set 2	0.964	0.991	0.920	0.0026 s	0.0072 s	2.8913 s

Numerical calculations of the fidelities $F_{\rm I}$ and $F_{\rm II}$ and related times t_m, t_μ, and t_ν concerning to the parameters of Set 1 and Set 2 for $M = 4$ and $P = 11$. As the values remain almost constant for $P\theta \in [0, \pi]$, varying less than 1%, we displayed here only the values corresponding to the phase $P\theta = \pi/2$, for fixed t_ν and t_μ. Set 1: $U/\hbar = 104.846$ Hz, $J/\hbar = 71.62$ Hz, $\mu/\hbar = 30.02$ Hz, and $t_{\rm m} \sim 6.16$ s. Set 2: $U/\hbar = 105.60$ Hz, $J/\hbar = 104.95$ Hz, $\mu/\hbar = 27.42$ Hz, and $t_{\rm m} \sim 2.89$ s. The required times t_m, $2t_{\rm m}$ to produce the NOON states are comparable with typical lifetimes of optical lattice traps, which can be as large as a few minutes[48].

Hamiltonian produces

$$|\Psi_1^{\rm II}\rangle = \frac{1}{2}\big(\beta|M,P,0,0\rangle + |M,0,0,P\rangle + |0,P,M,0\rangle - \beta|0,0,M,P\rangle\big);$$
$$|\Psi_2^{\rm II}\rangle = \frac{1}{2}\big(\beta|M,P,0,0\rangle + |M,0,0,P\rangle + i|0,P,M,0\rangle - i\beta|0,0,M,P\rangle\big);$$
$$|\Psi_3^{\rm II}\rangle = \frac{1}{\sqrt{2}}\Big(|M,P,0,0\rangle + \beta e^{-i\pi/2}|M,0,0,P\rangle\Big);$$
$$|\Psi_4^{\rm II}\rangle = \frac{1}{\sqrt{2}}(|M,P,0,0\rangle + \Upsilon|M,0,0,P\rangle)$$

where $\Upsilon = \beta\exp(i(P\theta - \pi/2))$.

Protocol fidelities. The analytic results provided above are obtained by employing the effective Hamiltonian in an extreme limit, with divergent applied fields acting for infinitesimally small times. Below we give numerical simulations of the protocols to show that, for physically realistic settings where the fields are applied for finite times, high-fidelity outcomes for NOON state production persist.

Throughout this section, we use $|\Psi\rangle$ to denote an analytic state, obtained in an idealized limit. We adopt $|\Phi\rangle$ to denote a numerically calculated state, obtained by time evolution with the EBHM Hamiltonian (2). Two sets of parameters are chosen to illustrate the results (expressed in Hz):

Set 1: $\{U/\hbar = 104.85,\ J/\hbar = 71.62,\ \mu/\hbar = 30.02\}$;
Set 2: $\{U/\hbar = 105.60,\ J/\hbar = 104.95,\ \mu/\hbar = 27.42\}$.

For all numerical simulation results presented below, the initial state is chosen as $|\Psi_0\rangle = |4,11,0,0\rangle$, i.e. $M = 4$ and $P = 11$.

The fidelities of Protocols I and II are defined as[40] $F_{\rm I} = |\langle\Psi_3^{\rm I}|\Phi_3^{\rm I}\rangle|$ and $F_{\rm II} = |\langle\Psi_4^{\rm II}|\Phi_4^{\rm II}\rangle|$, respectively. This is computed for $P\theta$ ranging from 0 to π, achieved by varying t_μ. In the case of Protocol II, we use $\nu = \mu$ for both sets of parameters. The systems considered here can, in principle, be implemented using existing hardware—see Physical proposal.

Illustrative results are presented in Table 1, where it is seen that $F_{\rm II}$ is lower than $F_{\rm I}$. This can be attributed to two primary causes. The first is that, while Protocol I takes $\tau_I \sim t_{\rm m}$ to produce the final state, Protocol II requires double the evolution time $\tau_{II} \sim 2t_{\rm m}$. The longer evolution time contributes to a loss in fidelity. The second reason is that, the measurement occurring in the final step of Protocol I has the effect of renormalizing the quantum state after the collapse, which increases the fidelity of the resulting NOON state when a measurement of $r = 0$ or $r = M$ is obtained. However, there is a finite probability that the measurement outcome is neither $r = 0$ nor $r = M$ (see Supplementary Note 2).

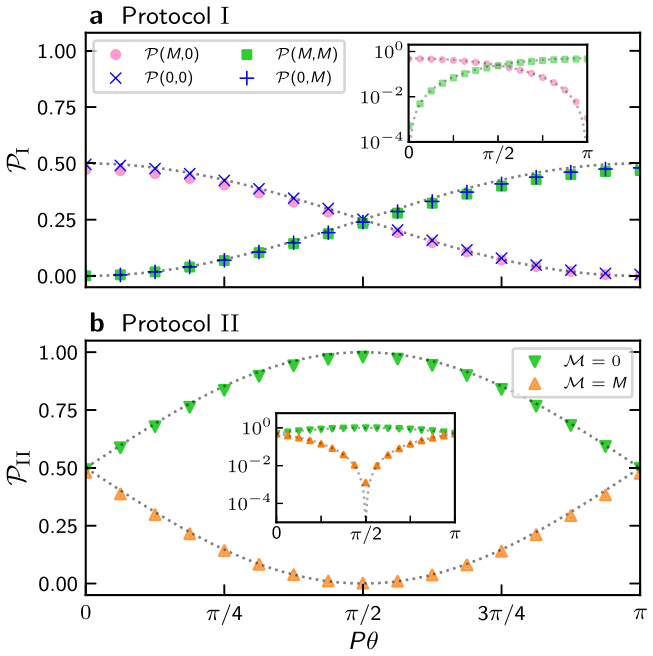

Fig. 2 Readout probabilities for Protocols I and II. Comparison between analytic and numerically calculated probabilities for parameters of Set 1 for different values of $P\theta$. **a** Results for Protocol I. The pink dot and the blue "x" (green square and the blue "+") depict the probabilities of measuring $r = 0$ ($r = M$) during the readout, having measured $r = M$ or $r = 0$ in step (iii), respectively. **b** Results for Protocol II. The probabilities of measuring $N_3 = 0$ ($N_3 = M$) in the readout are shown as green (orange) triangles. The dotted line depicts the analytic predictions of the probabilities with respect to $P\theta$. The insets show the accordance between predicted and calculated probabilities in semilogarithmic scale.

In summary, both protocols display high fidelity results greater than 0.9. For Protocol I the outcomes are probabilistic (See Supplementary Note 2 for data). By contrast, the slightly lower fidelity results of Protocol II are deterministic. These results also reflect the trade-off between fidelity and total evolution time. The higher fidelity results associated with parameter Set 1, compared to Set 2, are produced through a long evolution time.

Readout statistics. A means to test the reliability of the system, through a statistical analysis of local measurement outcomes, is directly built into the design. This results from the system's capacity to function as an interferometer[33]. For both protocols, once the output state has been attained we can continue to let the system evolve under $\mathcal{U}(t_{\rm m},0,0)$. This yields the readout states, denoted as $|\Psi_{\rm RO}^{\rm I}\rangle$, $|\Psi_{\rm RO}^{\rm II}\rangle$ respectively, for protocols I and II. In the idealized limits these are

$$|\Psi_{\rm RO}^{\rm I}\rangle = \begin{cases} \frac{c(\theta)}{\sqrt{2}}(|M,P,0,0\rangle + \beta|M,0,0,P\rangle) \\ +\frac{is(\theta)}{\sqrt{2}}(\beta|0,P,M,0\rangle - |0,0,M,P\rangle), & r = 0, \\ \frac{c(\theta)}{\sqrt{2}}(|M,P,0,0\rangle - \beta|M,0,0,P\rangle) \\ -\frac{is(\theta)}{\sqrt{2}}(\beta|0,P,M,0\rangle - |0,0,M,P\rangle), & r = M, \end{cases}$$

$$|\Psi_{\rm RO}^{\rm II}\rangle = \frac{1}{\sqrt{2}}s\Big(\theta - \frac{\pi}{2P}\Big)\big(|M,P,0,0\rangle + \beta|M,0,0,P\rangle\big) - \frac{i}{\sqrt{2}}c\Big(\theta - \frac{\pi}{2P}\Big)\big(\beta|0,P,M,0\rangle - |0,0,M,P\rangle\big),$$

where $c(\theta) \equiv \cos\big(P\theta/2\big)$ and $s(\theta) \equiv \sin\big(P\theta/2\big)$. For $|\Psi_{\rm RO}^{I}\rangle$, the measurement probabilities at site 3 are $\mathcal{P}(0) = \cos^2\big(P\theta/2\big)$ and

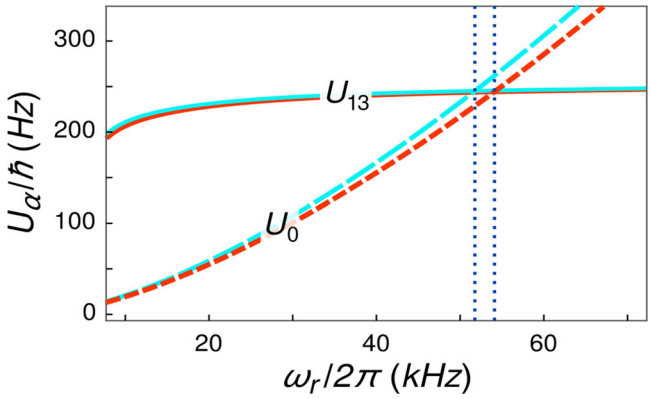

Fig. 3 Fulfillment of integrability condition. The s-wave scattering length value is set, followed by a variation of the radial trapping frequency ω_r up to the point at which $U_0 = U_{13}$, corresponding to the frequency required for the system to be integrable. The red dashed (solid) and cyan long dashed (solid) depict U_0 (U_{13}) for $a = 32.5\ a_0$ and $a = 30\ a_0$, respectively, for different values of ω_r. By setting $a = 32.5\ a_0$ ($30\ a_0$), we find $\omega_r \approx 2\pi \times 54.110$ kHz (51.759 kHz) as the frequency for integrability, which results in $U_0/\hbar = U_{13}/\hbar \approx 244.405$ Hz (245.141 Hz). The points where $U_0 = U_{13}$ and the corresponding frequencies ω_r are highlighted by the dotted lines. The system is robust for small deviations from the integrable point (see Supplementary Note 5 for more details).

$\mathcal{P}(M) = \sin^2(P\theta/2)$. Combined with the probability of measuring $r = 0, M$ in step (iii), we obtain four possibilities for the total probabilities as $\mathcal{P}_I(0,0) = \mathcal{P}_I(M,0) = 0.5\cos^2(P\theta/2)$ and $\mathcal{P}_I(0,M) = \mathcal{P}_I(M,M) = 0.5\sin^2(P\theta/2)$. Meanwhile, for $|\Psi^{II}_{RO}\rangle$, the measurement probabilities at site 3 are $\mathcal{P}_{II}(0) = \sin^2(P\theta/2 - \pi/4)$ and $\mathcal{P}_{II}(M) = \cos^2(P\theta/2 - \pi/4)$. As a numerical check, we consider the same sets of parameters as in the previous section. We numerically calculate the above probabilities using the Hamiltonian (2), comparing the predicted analytic results with the numerical ones, as shown in Fig. 2. See Supplementary Note 2 for numerical probabilities of Protocol I, and related fidelity data. For results with Set 2, see Supplementary Note 3.

Conclusions

We have addressed the challenging problem of designing protocols to facilitate NOON state creation. Our approach employs dipolar atoms confined to four sites of an optical superlattice. The setup allows for the interactions to be tuned, and to fix the couplings in such a way that the system is integrable. At these couplings, and for controlled perturbative breaking of the integrability, the theoretical properties of the system become very transparent.

The insights gained from integrability allowed us to develop two protocols utilizing a Fock-state input (see Supplementary Note 4). Protocol I employs a local measurement procedure to produce NOON states with slightly higher fidelities, over a shorter time, than Protocol II. However Protocol I is probabilistic, requiring post-selection on the measurement outcome. This is in contrast to the deterministic approach of Protocol II. For both protocols, phase-encoding is performed by breaking the system's integrability, in a controllable fashion, at specific moments during the time evolution. And in both protocols the output states were shown to have high-fidelity in numerical simulations. We also identified a readout scheme, by converting encoded phases into a population imbalance, that allows verification of NOON state production through measurement statistics.

The approaches we have described, which are based on the formation of an uber-NOON state en route to the final state, have two significant advantages. One is that the evolution time does not scale with the total number of particles. Instead, it is only dependent on the difference in particle number of subsystems A and B in the Fock-state input. The other advantage is that all measurements are made on a local Fock-state basis.

We conducted an analysis of the feasibility of a physical proposal. It was demonstrated that the long-range interaction between dipolar atoms allows for an integrable coupling to be achieved, depending on the interplay between contact and dipolar interactions. Through the second-quantization procedure the values for the Hamiltonian parameters were provided, derived by numerical calculations. These are seen to be realistic both in the context of optical lattice setups and in comparison to literature. We also conducted an analysis of the system's robustness in response to perturbation (see Supplementary Note 5 for a broader description).

Besides demonstrating the feasibility of NOON state generation, the physical setup we provide can also be employed in the study of thermalization processes and other many-body features of the EBHM. By establishing a link between integrability and quantum technologies, this work promotes advances in the field of neutral-atom quantum information processing.

Methods

Resonant tunneling regime. The Hamiltonian (2) has large energy degeneracies when $J = 0$. Through numerical diagonalization of the integrable Hamiltonian for sufficiently small values of J, it is seen that the levels coalesce into well-defined bands, similar to that observed in an analogous integrable three-site model[41,42]. By examination of second-order tunneling processes in this regime (see Supplementary Note 1), an effective Hamiltonian $H_{\rm eff}$ is obtained.

For an initial Fock state $|M-l, P-k, l, k\rangle$, with total boson number $N = M + P$, the effective Hamiltonian is a simple function of the conserved operators with the form

$$H_{\rm eff} = (N+1)\Omega(Q_1 + Q_2) - 2\Omega Q_1 Q_2, \tag{3}$$

where $\Omega = J^2/(4U((M-P)^2 - 1))$ and $U = (U_{12} - U_0)/4$. This result is valid for $J \ll U|M-P|$, and it is this inequality that we use to define the resonant tunneling regime.

A very significant feature is that, for time evolution under $H_{\rm eff}$, both $N_1 + N_3 = M$ and $N_2 + N_4 = P$ are constant. The respective $(M+1)$-dimensional subspace associated with sites 1 and 3 and $(P+1)$-dimensional subspace associated with sites 2 and 4 provide the state space for the relevant energy band (see Supplementary Note 1). Restricting to these subspaces and using the effective Hamiltonian (3) yields a robust approximation for (2).

Physical proposal. We propose a physical construction, consisting of ultracold dysprosium ^{164}Dy atoms trapped in an optical superlattice[35], to test the theoretical results. The trapping is accomplished by superimposing two 2D square optical lattices, one with "short" periodicity $\lambda/2$ and another with "long" periodicity $\lambda_l/2 = \lambda$, where the wavelength $\lambda = 2\pi/k = 532$ nm. The potential of the superlattice is given by

$$V(\mathbf{r}) = -V_s\sin^2(kx) - V_s\sin^2(ky) + V_l\sin^2(kx/2) + V_l\sin^2(ky/2) + \frac{1}{2}m\omega_z^2 z^2,$$

where V_s and V_l are the depths of the short and long lattices, respectively. The trap frequency $\omega_z = \sqrt{V_z k^2/(2m)}$ of the harmonic confinement in z direction is controlled by the depth V_z of vertical counter-propagating laser beams with wavelength $\lambda_l = 1064$ nm, and m is the atom's mass. We are interested in only one plaquette with four wells around the origin of the xy-plane, for which the potential of the ith well ($i = 1, 2, 3, 4$) in the harmonic approximation is given by

$$V^{(i)}(\mathbf{r}) = \frac{1}{2}m\omega_r^2[(x - x_i)^2 + (y - y_i)^2] + \frac{1}{2}m\omega_z^2 z^2, \tag{4}$$

where the radial trap frequency $\omega_r = \sqrt{2V_s k^2/m}$ is determined by the depth of the short lattice. The ith well is centered at one of the $(x_i, y_i) = (\zeta_{i-1}d/2, \zeta_i d/2)$, $\zeta_i \equiv (-1)^{\lfloor i/2 \rfloor}$, positions in the xy-plane. The distance between nearest wells is $d = \lambda/(2\delta)$, where the parameter $\delta = [1 - V_l/(2\pi V_s)]^{-1}$ is constant, which results from the harmonic approximation and causes the sites to slightly approach each other. In our studies we consider $V_l = V_s$.

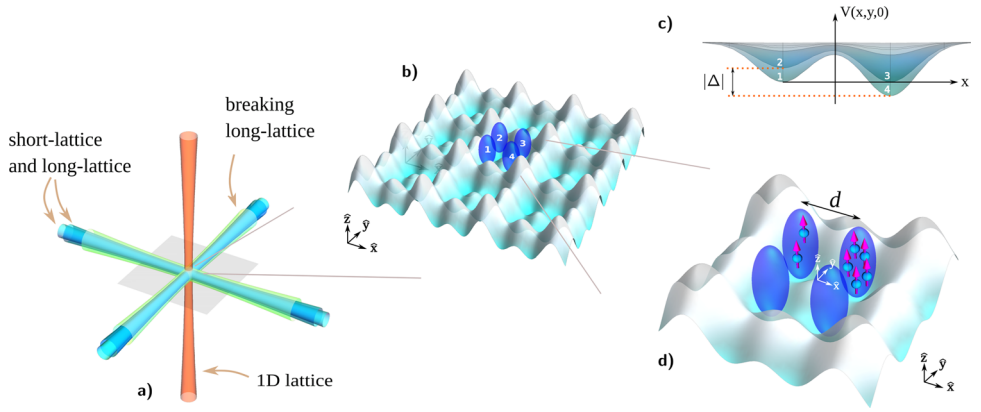

Fig. 4 Trapping scheme of the four-site model. a The 2D square optical lattice is generated with two sets of counter-propagating laser beams crossing at 90° with the other. The superlattice of the four-site model is achieved overlapping the 2D short-lattice (cyan) and long-lattice (blue). The vertical lattice (orange) provides confinement in *z* direction. An additional 2D square long-lattice (green) is used to implement the integrability break control. **b** Zoom into the region of the superlattice, which contains the four-site plaquette. **c** Breaking-of-integrability scheme. The system's integrability can be broken by changing the phase difference between the superlattice and the additional 2D square long-lattice, effectively causing a potential imbalance |Δ| between wells 1 and 3 or wells 2 and 4, as in the detail. **d** The light gray background represents the trapping potential in the vicinities of the four-well system. The cigar-shaped of isosurfaces of the ground-state density, at a distance of *d* between nearest neighbors, are depicted in blue with direction of dipole aligned in the *z*-direction represented by purple arrows.

To establish equivalency between $V(\mathbf{r})$ and the Hamiltonian of Eq. (2), we employ the standard second-quantization procedure. From this, we calculate the on-site interaction parameter U_0 as:

$$U_0 = U_{\text{contact}} + U_{\text{dip}} = \kappa\left(\frac{\eta}{\pi}\right)^{3/2}\left(g - \frac{C_{\text{dd}}}{3}f(\kappa)\right),$$

where the value of $\kappa^2 \equiv \omega_z/\omega_r = 0.53$ (0.56) establishes the cigar-shaped harmonic potential, $\eta \equiv m\omega_r/(2\hbar)$, $g \equiv 4\pi\hbar^2 a/m$, with a being the s-wave scattering length (tunable via Feshbach Resonance), $C_{\text{dd}} \equiv \mu_0\mu_1^2$ is the coupling constant, where μ_0 is the vacuum magnetic permeability, μ_1 is the atomic magnetic moment, and $f(\kappa)$ is a function that describes how the dipolar interaction behaves for different geometries (encoded in κ)[43]. Taking site 1 as the "starting point', the parameter U_{1j}, which accounts for the dipole-dipole interaction between atoms at sites 1 and j, is expressed as:

$$U_{1j} = \frac{C_{\text{dd}}}{4\pi}\int_0^\infty \mathrm{d}r r \exp\left(-\frac{r^2}{4\eta}\right) J_0(r d_{1j}) Z(r),$$

$$Z(r) = \left(\frac{4}{3}\sqrt{\frac{\kappa^2\eta}{\pi}} - r\exp\left(\frac{r^2}{4\kappa^2\eta}\right)\operatorname{erfc}\left(\frac{r}{2\sqrt{\kappa^2\eta}}\right)\right),$$

where J_0 is the Bessel function of first kind, $d_{1j} = \lambda/(2\delta)$, if $j = 2, 4$, and $d_{1j} = \lambda/(\sqrt{2}\delta)$, if $j = 3$. Here, the on-site dipolar interaction is given by $U_{\text{dip}} = \lim_{d_{ij}\to 0} U_{1j} \propto f(\kappa)$.

In this environment, the preparation of arbitrary initial Fock states, as in our protocols, may be accomplished[44,45] by changing one of the superimposed optical lattices' phase with respect to the other, creating imbalances in the trapping potentials in a controllable way, such that the desired initial state becomes favorable within a Mott Insulator regime (see Supplementary Note 4).

Integrability condition. The physical setup above is able to simulate the EBHM. The ability to generate NOON states, however, relies on the particular case for which the EBHM is integrable; as explained previously, this can be accomplished by making $U_0 = U_{13}$, which we call the "integrability condition". The approach is to first choose a value for the s-wave scattering length by changing the magnetic field. Then, from the condition just stated, one has to adjust ω_r by varying the laser beams intensities[46] such that, at some point, U_0 becomes the same as U_{13}. From this point every Hamiltonian parameter is evaluated only after the integrability condition is satisfied, which sets the intensity of the trapping scheme.

By considering $a = 32.5\ (30)\ a_0$, the system becomes integrable at $\omega_r \approx 2\pi \times 54.110$ ($2\pi \times 51.759$) kHz, as is depicted in Fig. 3. This frequency implies a 2D-lattice depth of $V_s \approx 39.953 E_R$ ($36.558 E_R$), where $E_R/\hbar = 2\hbar(k\pi)^2/(m\lambda^2) = 26.894$ kHz is the recoil energy, characterizing a deep lattice. This configuration infers a stable system[21,47]. Then, by using this trapping frequency to calculate the Hamiltonian parameters, one finds $U/\hbar \approx 104.846$ (105.600) Hz and $J/\hbar \approx 71.624$ (104.953) Hz.

It is also important to highlight that the tunneling parameter $J_{13}/\hbar \sim 3.2 \times 10^{-4}$ Hz ($J_{13}/\hbar \sim 7.7 \times 10^{-4}$ Hz) between diagonal sites 1–3, which is nullified by the condition $U_0 = U_{13}$ in (2), is less than $1/t_m \sim 0.16$ Hz ($1/t_m \sim 0.35$ Hz), relative to Set 1 (Set 2), ensuring the integrability requirement, considering $J_{13} = J_{24}$, since $U_0 = U_{13} = U_{24}$.

From this, one infers that the tunneling between different horizontal layers of the optical lattice is even smaller, since the distance between these layers is bigger than the distance between diagonal sites by a factor of $\sqrt{2}$.

Breaking of integrability. To produce a controllable breaking of integrability, it is sufficient to consider an additional 2D square long-lattice with the potential

$$V_{\text{break}} = V_b \sin^2(kx/2 + \varphi) + V_b \sin^2(ky/2 + \epsilon\varphi),$$

where the depth $V_b = 10^{-3} V_s$ and phase φ control the potential offset $\Delta = 2V_b \sin(2\varphi)\sin[\pi/(2\delta)]$ of sites 1–3 ($\epsilon = +1$) and 2-4 ($\epsilon = -1$). When this additional long-lattice is switched on, the depth of the fixed long-lattice is ramped down to $V_1 \to V_1 - V_b$ to keep the parameter δ constant and it implements the terms $\mu = 0.5\,\Delta\,\exp(-k^2/(8\eta_r))\,\delta_{\epsilon,+1}$ and $\nu = 0.5\,\Delta\,\exp(-k^2/(8\eta_r))\,\delta_{\epsilon,-1}$. For $\varphi = 15$ mrad and the previously obtained radial trapping frequency, the parameters $\mu/\hbar$ and $\nu/\hbar$ can (non-simultaneously) assume the value of 30.016 (27.415) Hz. Therefore, considering $M = 4$ and $P = 11$, one should vary t_μ from 0 to ~4.8(5.2) ms to encode $P\theta$ from 0 to π. Notice that for the case presented in Table 1, where $P\theta = \pi/2$, $t_\mu \sim 2.4(2.6)$ ms. Also, from the condition $2vt_\nu/\hbar = \pi/(2M)$, corresponding to $P\theta = \pi/2$, $t_\nu \sim 6.5(7.2)$ ms. Figure 4 illustrates the complete trapping scheme.

Data availability

All relevant data are available on reasonable request from the authors.

Code availability

Code used in the analysis is available from the authors upon reasonable request.

Received: 9 March 2021; Accepted: 14 January 2022;
Published online: 08 February 2022

References

1. Lee, H., Kok, P. & Dowling, J. P. A quantum Rosetta Stone for interferometry. *J. Mod. Opt.* **49**, 2325 (2002).
2. Afek, I., Ambar, O. & Silberberg, Y. High-NOON states by mixing quantum and classical light. *Science* **328**, 879 (2010).
3. Bollinger, J. J., Itano, W. M., Wineland, D. J. & Heinzen, D. J. Optimal frequency measurements with maximally correlated states. *Phys. Rev. A* **54**, R4649 (1996).
4. Boto, A. N. et al. Quantum interferometric optical lithography: exploiting entanglement to beat the diffraction limit. *Phys. Rev. Lett.* **85**, 2733 (2000).
5. Wildfeuer, C. F., Lund, A. P. & Dowling, J. P. Strong violations of Bell-type inequalities for path-entangled number states. *Phys. Rev. A* **76**, 052101 (2007).

6. Pan, J.-W. et al. Multiphoton entanglement and interferometry. *Rev. Mod. Phys.* **84**, 777 (2012).
7. Haas, J. et al. Chem/bio sensing with non-classical light and integrated photonics. *Analyst* **143**, 593–605 (2018).
8. Rarity, J. G. et al. Two-photon interference in a Mach-Zehnder interferometer. *Phys. Rev. Lett.* **65**, 1348 (1990).
9. Pryde, G. J. & White, A. G. Creation of maximally entangled photon-number states using optical fiber multiports. *Phys. Rev. A.* **68**, 052315 (2003).
10. Resch, K. J. et al. Time-reversal and super-resolving phase measurements. *Phys. Rev. Lett.* **98**, 223601 (2007).
11. Kamide, K., Ota, Y., Iwamoto, S. & Arakawa, Y. Method for generating a photonic NOON state with quantum dots in coupled nanocavities. *Phys. Rev. A* **96**, 013853 (2017).
12. Soto-Eguibar, F. & Moya-Cessa, H. M. Generation of NOON states in waveguide arrays. *Ann. Phys.* **531**, 1900250 (2019).
13. Merkel, S. T. & Wilhelm, F. K. Generation and detection of NOON states in superconducting circuits. *N. J. Phys.* **12**, 093036 (2010).
14. Hu, Y. M., Feng, M. & Lee, C. Adiabatic Mach-Zehnder interferometer via an array of trapped ions. *Phys. Rev. A* **85**, 043604 (2012).
15. Cable, H., Laloë, F. & Mullin, W. J. Formation of NOON states from Fock-state Bose-Einstein condensates. *Phys. Rev. A* **83**, 053626 (2011).
16. Lewis-Swan, R. J. & Kheruntsyan, K. V. Proposal for demonstrating the Hong-Ou-Mandel effect with matter waves. *Nat. Commun.* **5**, 3752 (2014).
17. Lopes, R. et al. Atomic Hong-Ou-Mandel experiment. *Nature* **520**, 66–68 (2015).
18. Cirac, J. I., Lewenstein, M., Mölmer, K. & Zoller, P. Quantum superposition states of Bose-Einstein condensates. *Phys. Rev. A* **57**, 1208 (1998).
19. Bychek, A. A., Maksimov, D. N. & Kolovsky, A. R. NOON state of Bose atoms in the double-well potential via an excited-state quantum phase transition. *Phys. Rev. A* **97**, 063624 (2018).
20. Vanhaele, G. & Schlagheck, P. NOON states with ultracold bosonic atoms via resonance- and chaos-assisted tunneling. *Phys. Rev. A* **103**, 013315 (2021).
21. Góral, K., Santos, L. & Lewenstein, M. Quantum phases of dipolar bosons in optical lattices. *Phys. Rev. Lett.* **88**, 170406 (2002).
22. Tonel, A. P., Ymai, L. H., Foerster, A. & Links, J. Integrable model of bosons in a four-well ring with anisotropic tunneling. *J. Phys. A Math. Theor.* **48**, 494001 (2015).
23. Kinoshita, T., Wenger, T. & Weiss, D. S. A quantum Newtonas cradle. *Nature* **440**, 900–903 (2006).
24. Liao, Y. et al. Spin-imbalance in a one-dimensional Fermi gas. *Nature* **467**, 567–569 (2010).
25. Pagano, G. et al. A one-dimensional liquid of fermions with tunable spin. *Nat. Phys.* **10**, 198–201 (2014).
26. Batchelor, M. T. & Foerster, A. Yang-Baxter integrable models in experiments: from condensed matter to ultracold atoms. *J. Phys. A Math. Theor.* **49**, 17 (2016).
27. Yang, B. et al. Quantum criticality and the Tomonaga-Luttinger liquid in one-dimensional Bose gases. *Phys. Rev. Lett.* **119**, 165701 (2017).
28. Breunig, O. et al. Quantum criticality in the spin-1/2 Heisenberg chain system copper pyrazine dinitrate. *Science Adv.* **3**, 12 (2017).
29. Wang, Z. et al. Experimental observation of Bethe strings. *Nature* **554**, 219–223 (2018).
30. Pilatowsky-Cameo, S. et al. Positive quantum Lyapunov exponents in experimental systems with a regular classical limit. *Phys. Rev. E* **101**, 010202(R) (2020).
31. Yao, N. Y. et al. Bilayer fractional quantum Hall states with ultracold dysprosium. *Phys. Rev. A* **92**, 033609 (2015).
32. Baier, S. et al. Extended Bose-Hubbard models with ultracold magnetic atoms. *Science* **352**, 6282 (2016).
33. Grün, D. S. et al. Integrable atomtronic interferometry. *arXiv* https://arxiv.org/abs/2004.11987 (2004).
34. Yang, B. et al. Observation of gauge invariance in a 71-site Bose-Hubbard quantum simulator. *Nature* **587**, 392–396 (2020).
35. Dai, H.-N. et al. Four-body ring-exchange interactions and anyonic statistics within a minimal toric-code Hamiltonian. *Nat. Phys.* **13**, 1195 (2017).
36. Fukuhara, T. et al. Spatially resolved detection of a spin-entanglement wave in a Bose-Hubbard chain. *Phys. Rev. Lett.* **115**, 035302 (2015).
37. Yamamoto, R. et al. Site-resolved imaging of single atoms with a Faraday quantum gas microscope. *Phys. Rev. A* **96**, 033610 (2017).
38. Schäfer, F., Fukuhara, T., Sugawa, S., Takasu, Y. & Takahashi, Y. Tools for quantum simulation with ultracold atoms in optical lattices. *Nat. Rev. Phys.* **2**, 411–425 (2020).
39. Okuno, D., Amano, Y., Enomoto, K., Takei, N. & Takahashi, Y. Schemes for nondestructive quantum gas microscopy of single atoms in an optical lattice. *N. J. Phys.* **22**, 013041 (2020).
40. Nielsen, M. A. & Chuang, I. L. *Quantum Computation and Quantum Information* (Cambridge Univ. Press, 2010).
41. Wilsmann, K. W., Ymai, L. H., Tonel, A. P., Links, J. & Foerster, A. Control of tunneling in an atomtronic switching device. *Commun. Phys.* **1**, 91 (2018).
42. Tonel, A. P., Ymai, L. H., Wilsmann, K. W., Foerster, A. & Links, J. Entangled states of dipolar bosons generated in a triple-well potential. *SciPost Phys. Core* **2**, 003 (2020).
43. Lahaye, T., Menotti, C., Santos, L., Lewenstein, M. & Pfau, T. The physics of dipolar bosonic quantum gases. *Rep. Prog. Phys.* **72**, 126401 (2009).
44. Yang, B. et al. Controlling and entangling ultracold atoms in optical lattices. *Science* **369**, 550–553 (2020).
45. Yang, B. et al. Observation of gauge invariance in a 71-site Bose-Hubbard quantum simulator. *Nature* **587**, 392–396 (2020).
46. Bloch, I. Ultracold quantum gases in optical lattices. *Nat. Phys.* **1**, 23–30 (2005).
47. Müller, S. et al. Stability of a dipolar Bose-Einstein condensate in a one-dimensional lattice. *Phys. Rev. A* **84**, 053601 (2011).
48. Gibbons, M. J., Kim, S. Y., Fortier, K. M., Ahmadi, P. & Chapman, M. S. Achieving very long lifetimes in optical lattices with pulsed cooling. *Phys. Rev. A* **78**, 043418 (2008).

Acknowledgements

D.S.G. and K.W.W. were supported by CNPq (Conselho Nacional de Desenvolvimento Científico e Tecnológico), Brazil. A.F. acknowledges support from CNPq—Edital Universal 430827/2016-4. A.F. and J.L. received funding from the Australian Research Council through Discovery Project DP200101339. J.L. acknowledges the traditional owners of the land on which The University of Queensland operates, the Turrbal and Jagera people. We thank Ricardo R. B. Correia and Bing Yang for helpful discussions. D.S.G. thanks Gabriele Natale for thoughtful conversations.

Author contributions

All authors contributed to the conceptualization of the project, and actively engaged in the writing of the manuscript. D.S.G., K.W.W., and L.H.Y. implemented the theoretical analyses of the model, detailed the physical proposal, and processed the numerical computations. J.L. and A.F. designed the research framework, and directed the program of activities.

Competing interests

The authors declare no competing interests.

Additional information

Supplementary information The online version contains supplementary material available at https://doi.org/10.1038/s42005-022-00812-7.

Correspondence and requests for materials should be addressed to Jon Links.

Peer review information *Communications Physics* thanks Junhua Zhang and the other, anonymous, reviewer(s) for their contribution to the peer review of this work.

Reprints and permission information is available at http://www.nature.com/reprints

Publisher's note Springer Nature remains neutral with regard to jurisdictional claims in published maps and institutional affiliations.

Open Access This article is licensed under a Creative Commons Attribution 4.0 International License, which permits use, sharing, adaptation, distribution and reproduction in any medium or format, as long as you give appropriate credit to the original author(s) and the source, provide a link to the Creative Commons license, and indicate if changes were made. The images or other third party material in this article are included in the article's Creative Commons license, unless indicated otherwise in a credit line to the material. If material is not included in the article's Creative Commons license and your intended use is not permitted by statutory regulation or exceeds the permitted use, you will need to obtain permission directly from the copyright holder. To view a copy of this license, visit http://creativecommons.org/licenses/by/4.0/.

© The Author(s) 2022